Decay of secondary motion downstream bends in turbulent pipe flows

Bilde, Kasper Gram; Sørensen, Kim; Hærvig, Jakob

Published in:
Physics of Fluids

DOI (link to publication from Publisher):
10.1063/5.0129339

Publication date:
2023

Document Version
Early version, also known as pre-print

Decay of secondary motion downstream bends in turbulent pipe flows

Kasper Gram Bilde, Kim Sørensen, and Jakob Hærvig
AAU Energy, Aalborg University, 9220 Aalborg

(*Electronic mail: kgb@energy.aau.dk)

(Dated: 13 January 2023)

Decay of secondary motion downstream 180° pipe bends are investigated using Large Eddy Simulations (LES) for bend radii of $1 \leq r_B/d_h \leq 3.375$ at a Reynolds number of $Re_h = 10,000$. The velocity and turbulence characteristics are validated against experimental data for a straight pipe section as well as against experimental- and DNS data for a 90° pipe bend. As the bend radius decreases, a larger magnitude of turbulence intensity is induced immediately downstream of the bend and for the largest magnitude, the highest gradient of the decay turbulence intensity is observed. As a result, the recovery length needed to re-establish the velocity profile downstream of the pipe bend decreases. Turbulence is transported at a higher rate, indicating that the recovery of the velocity profile is driven by turbulence transport. Secondary motions are induced by the curvature of the pipe bend and as the bend radius decreases, the magnitude of the secondary motion increases. The results show how the secondary motion decay in magnitude as the flow moves downstream the pipe bend. At the outlet of the bend, secondary motions are dominating at the walls and within the bulk flow. As the fluid moves further downstream, the secondary flows dominate close to the walls and at a length of $x/d_h = 5$, a negligible difference in secondary motion is observed for the different bend radii.

I. INTRODUCTION

Transport of fluids in circular pipes is a part of most engineering applications and most often the fluid flow is in the turbulent regime. These applications include heat exchangers, chemical reactors, mixing devices and piping to and from various applications. For practical reasons the piping layout of the applications often includes both 90° and 180° pipe bends, where swirl, secondary motions and turbulence are induced downstream, which causes additional pressure losses and distorts the velocity profile[1]. The characteristics of turbulence and secondary motions downstream of a bend are important parameters for various applications when, e.g., measuring the volumetric flow rate using an electromagnetic flowmeter. The distorted velocity profile, due to the pipe bend, may result in both systematic and random errors[2].

Rowe (1970)[3] was among the first to study the total pressure distribution throughout a 180° pipe bend and analysed the downstream effect of the pipe bend. Experimental measurements were performed on a 180° circular pipe bend with a bend radius of $r_B = 12d_h$ and Reynolds number of $Re_h = 23,600$. Secondary flow patterns induced by a pipe bend were some of the main findings and it was concluded that the secondary flow was most intense at an angle of about 30° through the pipe.

Azzola et al. (1986)[4] extended the experimental work by measuring the longitudinal and azimuthal velocity components using laser Doppler velocimetry (LDV) for a 180° pipe bend with a bend radius of $r_B = 3.375d_h$ for Reynolds numbers of $Re_h = 57,400$ and $Re_h = 110,000$. Numerical results of the turbulence characteristics over the pipe bend were compared to the presented experimental results and the Reynolds stress tensor was modelled using the standard k-ε turbulence model[5]. It was reported that the numerical- and experimental results were in good agreement along the curvature of the pipe bend, but that the downstream results from the numerical model deviated from the experimental data.

Sudo et al. (2001)[6] measured the velocity components in a 180° pipe bend with a bend radius of $r_B = 4d_h$ for a Reynolds number of $Re_h = 60,000$ using hot-wires in a similar setup to Sudo et al. (1998)[7], who investigated the velocity profile through a 90° bend. It was reported that a recovery length of $x/d_h = 10$ was required to recover the symmetrical velocity profile for a 90° bend with a bend radius of $r_B = 4d_h$. Analysing the experimental results for the 180° pipe bend, it was concluded that the recovery length is longer for a 180° bend when compared to the 90° with similar inlet boundary conditions.

To achieve a better understanding of the downstream induced flow structures, Hellström et al. (2013)[8] used time-resolved stereoscopic particle image velocimetry (PIV). The experimental results were obtained for a 90° pipe bend for Reynolds numbers of $Re_h = 20,000$ and $Re_h = 115,000$. It is reported that the recovery of the profiles appears to be driven by turbulent transport, which is expected to be more significant at higher Reynolds numbers.

Di Liberto et al. (2013)[9] simulated the turbulent flow through a pipe with three bend radii, $r_B = 1.67d_h$, $r_B = 5d_h$ and $r_B = \infty$ (straight pipe), using direct numerical simulations (DNS). The authors simulated the flow with a constant friction Reynolds number of $Re_\tau = 500$, resulting in Reynolds numbers of $Re_h = 17,000$, $Re_h = 15,000$ and $Re_h = 12,000$ respectively. The domain was meshed using periodic boundary conditions, effectively giving an infinitely long curved pipe. The velocity profile within the pipe bend was reported with high accuracy as the smallest scale turbulence was resolved, but as an infinitely long pipe was simulated, the downstream effect was not in the scope of the study.

Röhrig et al. (2015)[10] studied the characteristics of a turbulent flow through a 90° pipe bend at Reynolds numbers between $14,000 \leq Re_h \leq 34,000$ using both a RANS model and a large-eddy simulation (LES) to resolve and model the turbulence in the flow. The LES model successfully captured the time-averaged velocity profile, secondary motions and turbulence structures, whereas the RANS model generally underpredicted the velocity at the walls. The higher accuracy of the

LES model comes at a higher computational cost when compared to the RANS model.

More recently, Gotfredsen et al. (2020)[11] measured the velocity profile and concentration profile of a tracer gas downstream of a 90° pipe bend using LDV. Numerical results of two different Reynolds averaged Navier-Stokes (RANS) using the k-ω SST and the k-ε turbulence models as well as results from a detached eddy simulation (DES) were compared to the experimental results. It was concluded that the k-ω SST model had difficulties when predicting the turbulence downstream and that the k-ε model produced better results except for the inlet of the 90° pipe bend. The DES model was successful in predicting the flow profile and turbulence up and downstream from the pipe bend.

In this study, the downstream flow characteristics of a 180° pipe bend are studied to evaluate the secondary motions, velocity fluctuations and turbulence induced by the bend. The time-averaged velocity profile and the recovery of this are also analysed in the present study to understand the recovery length needed to re-establish the velocity profile. The flow in the pipe is simulated for a Reynolds number of $\mathrm{Re_h} = 10,000$ using LES to resolve the velocity fluctuations. To analyse the effect of the bend radius of the 180° pipe bend, the flow characteristics are analysed for bend radii bounded by $d_\mathrm{h} \leq r_\mathrm{B} \leq 3.375 d_\mathrm{h}$.

II. DETAILS ON NUMERICAL SETUP

A. Geometrical configuration

The computational domain is seen in Fig. 1, where the bend radius of the pipe bend is denoted by $r_\mathrm{B} = k\,d_\mathrm{h}$. Upstream of the 180° bend, a pipe with a length of $x = 10d_\mathrm{h}$, is seen to make sure that a fully-developed turbulent velocity profile enters the pipe bend. Downstream from the bend, another straight pipe section of $x = 10d_\mathrm{h}$ is applied to analyse the downstream turbulent properties of the fluid flow.

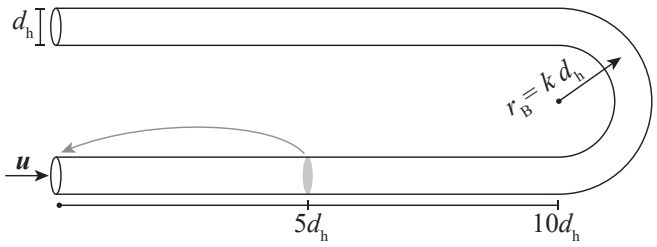

FIG. 1: Representation of the geometrical configuration with a bend radius of $r_\mathrm{B} = k\,d_\mathrm{h}$. The inlet velocity profile is mapped at $x = 5d_\mathrm{h}$ downstream and reapplied at the inlet.

B. Governing equations for the fluid flow

The filtered LES equations applied in this study are valid for an unsteady, incompressible, three-dimensional viscous flow and the continuity- and momentum equations are given by Eq. (1) and (2), respectively, as

$$\nabla \cdot \overline{\boldsymbol{u}} = 0\,, \tag{1}$$

$$\frac{\partial \overline{\boldsymbol{u}}}{\partial t} + \nabla \cdot (\overline{\boldsymbol{u}}\overline{\boldsymbol{u}}) = -\frac{1}{\rho}\nabla \overline{p} + \nabla \left(\left(\nu + \nu_\mathrm{sgs} \right) \nabla \cdot \overline{\boldsymbol{u}} \right)\,, \tag{2}$$

where $\overline{\boldsymbol{u}}$ is the filtered velocity, $\overline{p}$ is the filtered pressure, ν is the fluid viscosity and ν_sgs is the sub-grid scale turbulent viscosity. A pressure correction term is applied to the inlet boundary condition to balance the mean fluid velocity, as the velocity profile at the inlet is re-applied from a distance of $x = 5d_\mathrm{h}$ downstream from the inlet which is further described in section II E and illustrated in Fig. 1.

The governing equations are discretised using the finite volume method and time advancements are performed using an implicit, second-order accurate scheme where a maximum Courant–Friedrichs–Lewy (CFL) condition of $\mathrm{CFL} = \Delta x / (|\overline{\boldsymbol{u}}|\,\Delta t) < 1$ is restraining the time step advancements. All spatial terms are discretised using second-order accurate schemes to reduce numerical damping of the velocity fluctuations. The coupling of the pressure and velocity fields is performed using the PISO algorithm proposed by Issa (1986)[12]. All simulations in this study are carried out using the open-source CFD library OpenFOAM.

C. Sub-grid scale turbulence modelling

The sub-grid scale (SGS) turbulent viscosity, ν_sgs, is modelled using the wall-adapting local eddy-viscosity (WALE) model, proposed by Nicoud and Ducros (1999)[13], to account for the sub-grid scale eddy dissipation. The SGS model is given as

$$\nu_\mathrm{sgs} = \left(C_W V^{1/3} \right)^2 \frac{\left(\overline{s}^d_{ij} \overline{s}^d_{ij} \right)^{3/2}}{\left(\overline{s}_{ij} \overline{s}_{ij} \right)^{5/2} + \left(\overline{s}^d_{ij} \overline{s}^d_{ij} \right)^{5/4}}\,. \tag{3}$$

Herein, V is the volume of the local control volume and $C_W = 0.325$. The traceless symmetric part of the square of the velocity gradient tensor is defined as

$$\overline{s}^d_{ij} = \frac{1}{2}\left(\overline{g}^2_{ij} + \overline{g}^2_{ji} \right) - \frac{1}{3}\delta_{ij}\overline{g}^2_{kk}\,, \tag{4}$$

where δ_{ij} is the Kronecker delta, $\overline{s}_{ij}$ is the strain-rate tensor and the $\overline{g}_{ij}$ is the velocity gradient defined as $\overline{g}_{ij} = \partial \overline{u}_i / \partial x_j$.

When comparing the WALE model to the traditional Smagorinsky-type SGS turbulence models, the WALE model is well-suited for wall-bounded flows such as a pipe flow, as the SGS viscosity automatically goes to zero at the wall, resulting in no damping functions or dynamic constant adjustments to correct for the wall.

D. Computational domain

To resolve the largest turbulent eddies within the flow field, a fine computational mesh is required. The first cell height, contacting the wall surface, is placed at $y^+ = \Delta y u_\tau / \nu = 1$ for all applied meshes to accurately resolve the viscous sub-layer part of the boundary layer. The frictional velocity, u_τ, denotes the velocity at the wall. The largest cell height, $\Delta y_{\max}$, is placed in the centre of the pipe, as seen in the cross-sectional view of the pipe in Fig. 2, where a quarter of the cross-sectional view of the computational mesh is seen. The mesh is constructed with a maximum angle of 120° between each cell to ensure a high grid quality.

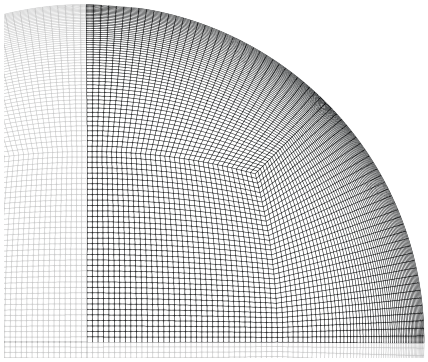

FIG. 2: Cross-sectional view of a quarter of the round pipe mesh.

For the different simulations carried out in the present study, the total number of computational cells varies between $29.7 \cdot 10^6$ and $38.7 \cdot 10^6$ depending on the bend radius. Simulations are carried out on an AMD EPYC 7V73X processor with 120 CPU cores and 448 GB of RAM. Simulation time is in the order of 40 hours per simulation.

E. Boundary conditions

A fully-developed turbulent velocity profile is applied to the inlet of the domain by re-applying the 3-dimensional velocity field at a distance of $x = 5d_\mathrm{h}$ downstream of the inlet, which is also illustrated in Fig. 1. The instantaneous velocity of the downstream patch is re-applied to the inlet boundary at the next time advancement and the pressure is corrected to ensure a mean velocity corresponding to the specified Reynolds number. This effectively creates an infinitely long straight upstream of the pipe bend with the sole purpose of creating a fully-developed turbulent velocity profile. To make sure no spatial correlations exist in the flow field from the inlet to the mapping plane, Robinson (1991)[14] suggests turbulence structures in pipe flow to extend $L_x^+ = 1000$ in viscous units while Hærvig et al. (2018)[15] used a computational domain of length $L_x^+ = 2500$ (corresponding to $L/d_\mathrm{h} = 4$) for a pipe flow with $\mathrm{Re_h} = 10,000$. The velocity field is therefore updated each time step to account for both spatial and temporal changes in the velocity profile. Uniform pressure is applied at the outlet of the domain and the *no-slip* velocity condition is applied to all walls.

F. Validation

The near-wall velocity profile of the straight pipe section is compared to experimental results obtained by Toonder and Nieuwstadt (1997)[16] for a straight pipe section. The velocity, normalised by the friction velocity $u_\tau = \sqrt{\tau/\rho}$, is evaluated downstream at a length of $x = 5d_\mathrm{h}$ relative to the inlet, which is also where the instantaneous velocity is re-applied to the inlet at every time advancement.

The numerical results obtained for three different mesh densities are compared to the experimental values of Toonder and Nieuwstadt (1997)[16] in Fig. 3 and 4. The absolute and RMS velocities are normalised using the frictional velocity, u_τ, for the straight section of the pipe and it is found that the LES data is in good agreement with both the experimental data and also the theoretical law of the wall[17]. The finest mesh is in good agreement with both the streamwise velocity and the axial RMS velocity, however, it overpredicts the radial RMS velocity close to the wall, as seen in Fig. 4b. The LES results are in good agreement with the radial RMS velocity when the flow moves further away from the wall. As the finest mesh is in good agreement with the experimental data and this grid density is chosen as the mesh size for the following results presented in this study.

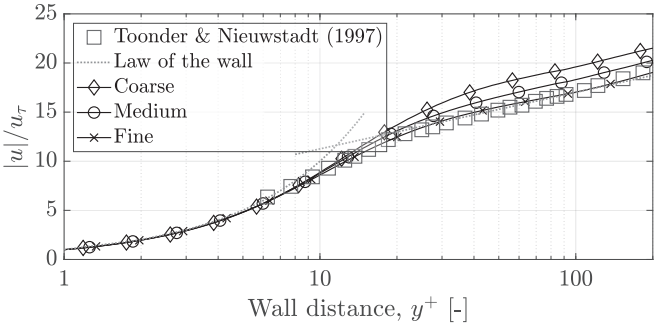

FIG. 3: Normalised velocity, $|\boldsymbol{u}|/u_\tau$, as functions of the dimensionless boundary layer, distances to the wall y^+ for the straight pipe flow compared to experimental results obtained by Toonder and Nieuwstadt (1997)[16] and to the law of the wall (viscous sub-layer $u^+ = y^+$ and log-law layer $u^+ = 2.5 \cdot \ln(y^+) + 5.5$).

For validation purposes only, simulations through a 90° bend at $\mathrm{Re_d} = 5300$ and $\mathrm{Re_d} = 14000$ is carried out using the LES model and the results are compared against DNS data by Wang et al. (2018)[18] as well as experimentally obtained data using combined Particle Image Velocimetry (PIV) and Hot-Wire (HW) by Sattarzadeh (2011)[19] and Kalpakli et al. (2016)[20]. The DNS data of Wang et al. (2018)[18] is obtained for a 90° bend of $r_\mathrm{B} = 1.25d_\mathrm{h}$ for a fluid flow of $\mathrm{Re_d} = 5300$. The normalised velocity profile is in good agreement with the DNS data, as shown in Fig. 5a. The PIV-HW data of both Sattarzadeh (2011)[19] and Kalpakli et al. (2016)[20] is obtained

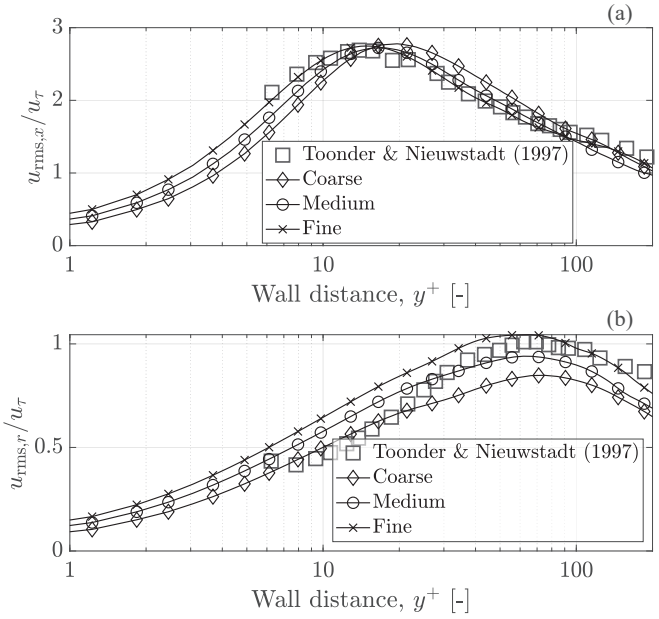

FIG. 4: Normalised RMS velocity for the three mesh densities compared to experimental data of Toonder and Niuewstadt (1997)[16] for the straight pipe section. The normalised axial RMS velocity, $u_{\mathrm{rms},x}/u_\tau$, is shown in Fig. 4a and the normalised radial RMS velocity, $u_{\mathrm{rms},r}/u_\tau$, is shown in Fig. 4b.

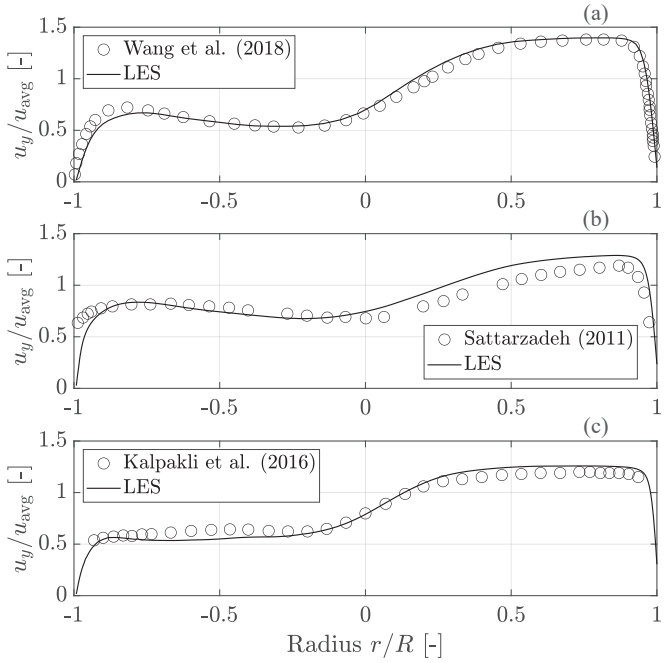

FIG. 5: The normalised streamwise velocity, $u_{\mathrm{y}}/u_{\mathrm{avg}}$, for a pipe with a 90° bend. The streamwise velocity for $\mathrm{Re_d} = 5300$ and $r_{\mathrm{B}} = 1.25d_{\mathrm{h}}$ are compared to the DNS data of Wang et al. (2018)[18] in Fig. 5a. The streamwise velocity for $\mathrm{Re_d} = 14000$ and $r_{\mathrm{B}} = 1.58d_{\mathrm{h}}$ is compared to PIV-HW data of Sattarzadeh (2011)[19] and Kalpakli et al. (2016)[20] measured at a downstream length of $x/d_{\mathrm{h}} = 1.5$ in Fig. 5b and at a downstream length of $x/d_{\mathrm{h}} = 0.67$ in Fig. 5c.

for a 90° bend of $r_{\mathrm{B}} = 1.58d_{\mathrm{h}}$ at a flow of $\mathrm{Re_d} = 14000$. Sattarzadeh (2011)[19] reports the data at a downstream length of $x/d_{\mathrm{h}} = 1.5$ whereas Kalpakli et al. (2016)[20] report the data at a downstream length of $x/d_{\mathrm{h}} = 0.67$. The normalised streamwise velocity profile is in good agreement with the experimental data at both locations, as shown in Fig. 5b and 5c.

Sattarzadeh (2011)[19] and Kalpakli et al.[20] report the turbulence intensity downstream of the 90° bend and the results at the downstream location of $x/d_{\mathrm{h}} = 1.5$ is seen in Fig. 6a and at a downstream location of $x/d_{\mathrm{h}} = 0.67$ in Fig. 6b. It is observed that the LES model overpredicts the turbulence intensity slightly at the inner radius, $r_{\mathrm{B}} < 0$, however, the data is in good agreement with the experimental data. The turbulence intensity measured at the outer radius is in very good agreement with the experimental data.

Comparing the LES results to the experimental results for the straight pipe section in Fig. 3 and to the DNS and experimental data for a 90° pipe bend, it is shown that the LES model produces results that are in good agreement with both experimental and DNS data.

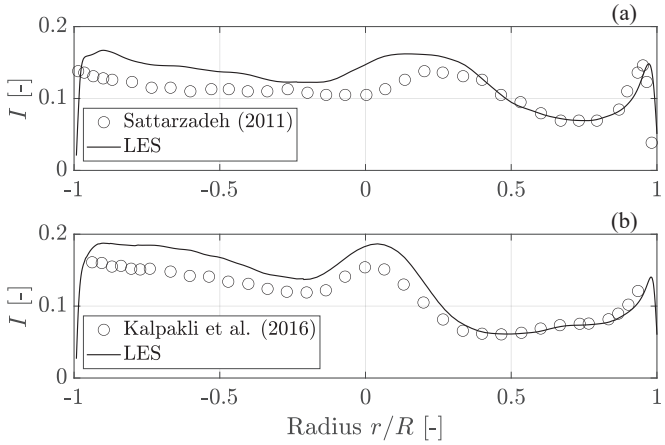

FIG. 6: Turbulence intensity for a 90° bend with a fluid flow of $\mathrm{Re} = 14000$ measured at a downstream location of $x/d_{\mathrm{h}} = 1.5$ in Fig. 6a and $x/d_{\mathrm{h}} = 0.67$ in Fig. 6b

III. RESULTS AND DISCUSSION

Five simulations are performed at $\mathrm{Re_h} = 10,000$ with bend radii in the range of $d_{\mathrm{h}} \leq r_{\mathrm{B}} \leq 3.375d_{\mathrm{h}}$. The number of computational cells applied in the computational domain is dependent on the bend radius, as the total length of the domain increases as the bend radius increases. A total of 29.7 million computational cells are applied for the smallest bend radius, $r_{\mathrm{B}} = d_{\mathrm{h}}$, and a total of 38.7 million computational cells are applied for the largest bend radius, $r_{\mathrm{B}} = 3.375d_{\mathrm{h}}$.

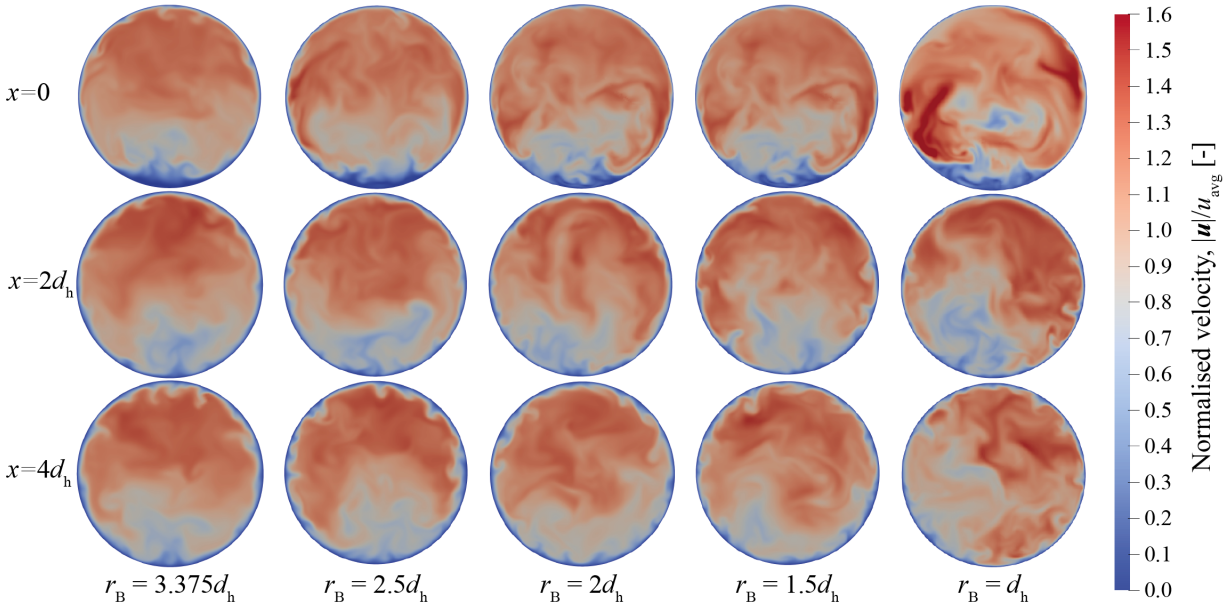

FIG. 7: Cross-sectional instantaneous normalised velocity contours for all bend radii at lengths of $x = 0$, $x = 2d_h$, $x = 4d_h$ downstream the 180° bend.

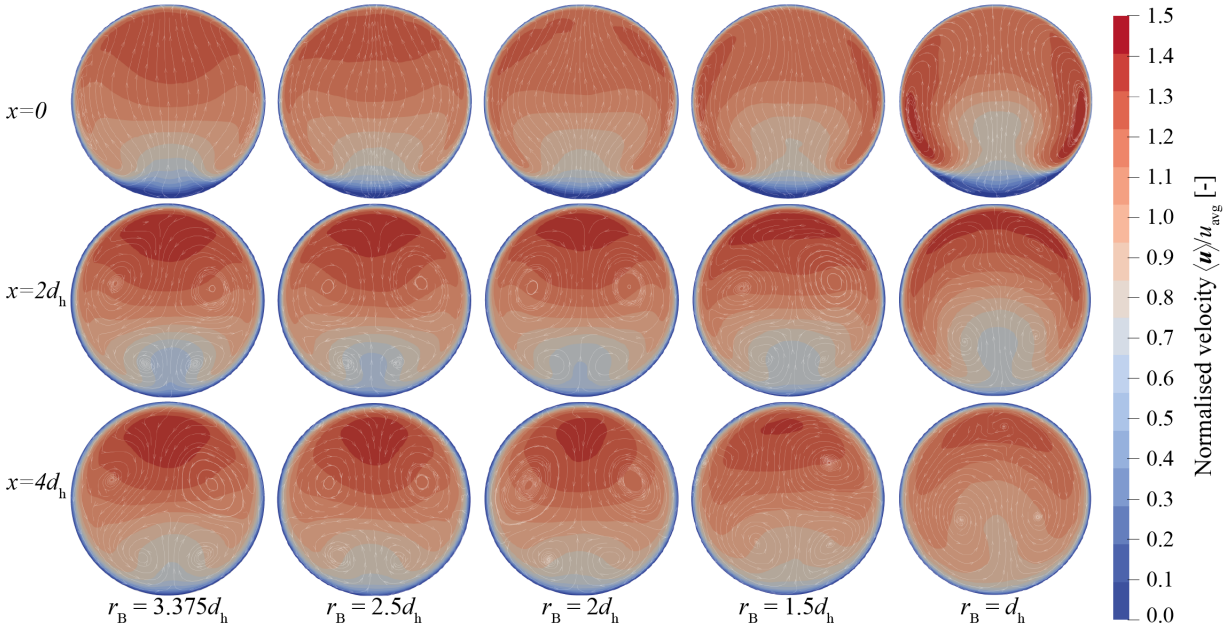

FIG. 8: Normalised velocity, $\langle \boldsymbol{u} \rangle / u_{\text{avg}}$, at lengths of $x = 0$, $x = 2d_h$ and $x = 4d_h$ downstream of the bend for different bend radii. The secondary flows are visualised as streamlines.

A. Instantaneous velocity fields

Instantaneous velocity contours of the cross section after the pipe bend are seen in Fig. 7, where the magnitude of the velocity is scaled by the bulk velocity of the flow. The contours are shown at a length of $0 \leq x \leq 4d_h$ downstream of the 180° bend to highlight the instantaneous velocity profile and the turbulence induced by the curvature of the bend. It immediately indicates that the smallest bend radius, $r_B = d_h$ induces the largest magnitude of velocity fluctuations, as this contour has the largest magnitude of velocity.

As the bend radius increases, it is seen how the velocity fluctuations decrease in magnitude and that the majority of the mass flow rate is located at the top half of the pipe. As the fluid moves downstream for the pipe, it is indicated that the velocity profile starts to recover, as the contours take a more

homogeneous colour at $x = 4d_h$ for all configurations when compared to $x = 0$.

B. Time-averaged velocity profiles

The instantaneous velocity contours provide insight into the velocity fluctuations in a very brief time period, which is why the time-averaged velocity profile provides a better understanding of the flow phenomena taking place downstream of the bend. The normalised time-averaged velocity, $\langle \boldsymbol{u} \rangle / u_{avg}$, is evaluated in the same cross-sectional planes as the instantaneous contours in Fig. 7 and the contours are shown in Fig. 8. The time-averaged velocity shows that a low-velocity zone is observed at the bottom of the pipe immediately after the bend, $x = 0$, for all bend radii. The low-velocity area is the largest for the smallest bend radius, $r_B = d_h$, which is due to the fluid streamlines slipping the wall due to the large curvature of the bend. The secondary flow streamlines are also visualised in Fig. 8 and it is observed for all cases that Dean vortices are induced by the pipe bend, which is also reported by other researchers.[21–23] The secondary flow profile is further described in section III C.

The time-averaged velocity profiles are evaluated in intervals of $\theta = 45^\circ$ between $0^\circ \leq \theta \leq 180^\circ$ throughout the 180° bend for the different bend radii and shown in Fig. 9. The inner radius of the pipe is denoted with $r/R = -1$ and the outer radius of the pipe is denoted with $r/R = 1$. It is seen that the velocity profile is skewed at the inlet of the pipe bend for the simulations with the smallest bend radius, $d_h \leq r_B \leq 1.5d_h$. The velocity profile continues to become more skewed throughout the bend and the biggest difference between the velocity profiles is observed at an angle of $\theta = 45^\circ$ through the bend. When the flow leaves the bend at an angle of $\theta = 180^\circ$, there is only a small difference between the normalised velocity profiles produced by the different bend radii.

The streamwise velocity for the symmetrical plane from the outlet of the pipe bend to the outlet of the computational domain is plotted in Fig. 10 to analyse the skewness and the recovery of the velocity profile downstream of the pipe bend. The velocity profile is normalised using the bulk velocity and plotted at a length of $x/d_h = 0$, $x/d_h = 2$, $x/d_h = 4$, $x/d_h = 6$ and $x/d_h = 8$ in Fig. 10a to 10e, respectively. It is observed that the skewed velocity profile that exits the pipe bend, as seen in Fig. 9 at an angle of $\theta = 180^\circ$, becomes even more skewed at a length of $x = d_h$ downstream from the bend, in Fig. 10a. The velocity profile for the smallest bend radius is the most skewed velocity profile at this location. When the fluid moves further downstream from the bend, the velocity profile starts to recover and at the outlet of the domain, seen in Fig. 10e, the most skewed velocity profile is observed for the simulation with the largest bend radius, $r_B = 3.375d_h$.

To quantify the skewness of the velocity profile over the cross-section of the pipe, the uniformity index, φ, of the velocity profile is evaluated, where the uniformity index is given by

$$\varphi = 1 - \frac{1}{2Au_{avg}} \int \left| \langle \boldsymbol{u} \rangle - u_{avg} \right| \mathrm{d}A \,. \tag{5}$$

A uniformity index of $\varphi = 1$ equals a uniform flow profile. The evolution of the uniformity index of the time-averaged velocity downstream of the pipe bends is shown in Fig. 11.

A relatively high uniformity index is observed at the outlet of the bend, $x = 0$ for all simulations. After a length of $x = d_h$, a drop is observed for all bend radii and this is where the flow experiences the lowest uniformity index. This is due to the fluid slipping the wall at the outlet as it cannot stay attached to the wall. Comparing the velocity profiles at the outlet of the bend in Fig. 9 and at a distance of $x = d_h$ in Fig. 10 show that a lower velocity occurs in the bottom part of the pipe due to the fluid flow not staying attached to the wall, causing the uniformity index to decrease in value. As the fluid moves further downstream from the bend, an increasing value for the uniformity index is observed, which is also qualitatively observed in Fig. 10. It is noteworthy to mention that the uniformity index for the simulation with the smallest bend radius reaches the overall lowest uniformity index of $\varphi = 0.87$ but increases in uniformity faster compared to the other configurations. In general, it is observed that the uniformity index increases faster when the bend radius decreases and the lowest uniformity index at $x = 10d_h$ are observed for the largest bend radius.

C. Decay of secondary motion

The secondary motion, also seen as flow streamlines in Fig. 8, is further analysed to study how the secondary flow decays as the flow moves downstream from the pipe bend. The secondary velocity is normalised using the bulk velocity as $(|u_y| + |u_z|)/u_{avg}$ and the secondary velocities are shown in Fig. 13 for the different bend radii. The secondary flow is largest in magnitude as the flow leaves the 180° bend which is seen in Fig. 13a. At this location, it is observed that the simulations for bend radii in the range of $d_h \leq r_B \leq 2.5d_h$ have two peaks which are at magnitudes of the same order. The first peak is observed closer to the wall, where a large secondary flow is present and a second peak is observed when moving towards the centre of the pipe.

When the fluid has moved a length of $x = d_h$ downstream of the bend, it is observed that the secondary flow has decreased significantly in magnitude, as seen in Fig. 13b. The secondary flow is now largest in magnitude close to the wall for all bend radii and the simulation with the smallest bend radii has the largest magnitude of secondary flow. This is the case until a length of $x = 4d_h$ downstream of the bend, seen in Fig. 13e, is reached, where it is observed that the secondary flow is still largest in magnitude for the smallest bend radius, but that the secondary flow is at a magnitude with small difference between the simulations.

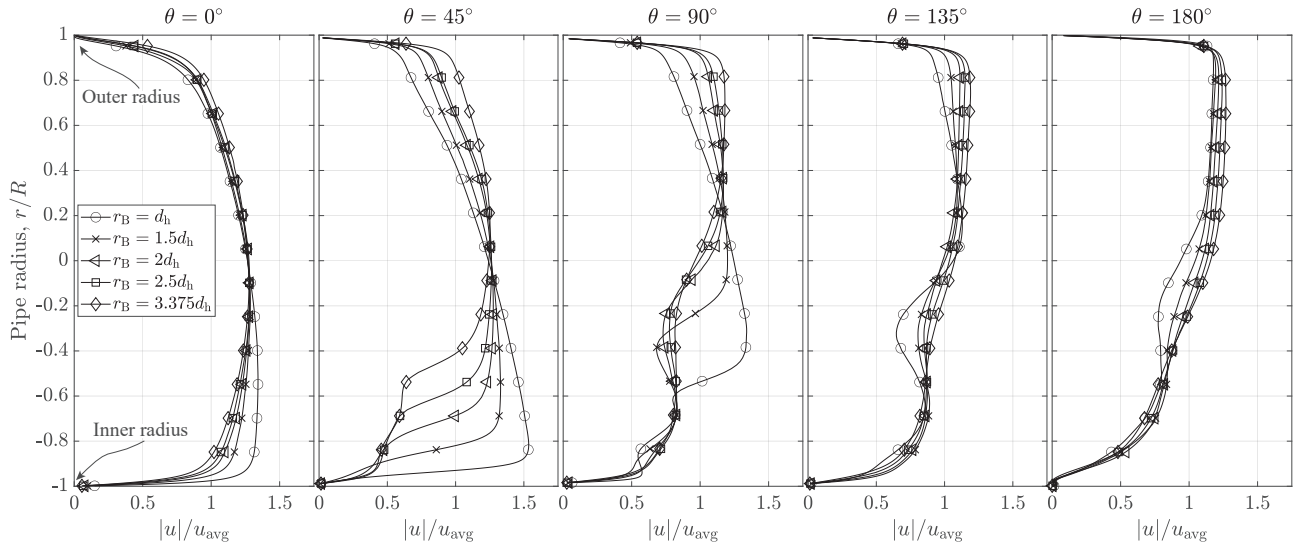

FIG. 9: Normalised velocity profile $|\boldsymbol{u}|/u_{\text{avg}}$ throughout the 180° bend for angles between $0^\circ \leq \theta \leq 180^\circ$. The inner bend is denoted with $r/R = 1$ and the outer bend is denoted with $r/R = -1$.

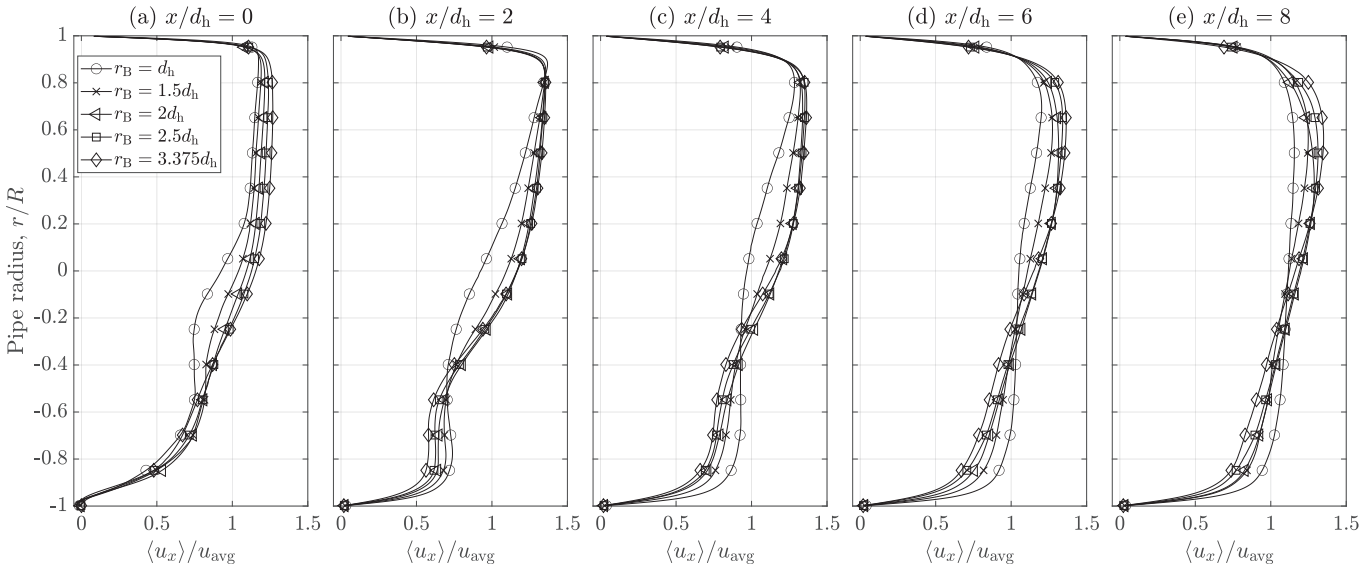

FIG. 10: Normalised streamwise velocity profile downstream of the pipe bend for the geometrical symmetry plane of the pipe at downstream lengths of $x/d_{\text{h}} = 0$ in Fig. 10a, $x/d_{\text{h}} = 2$ in Fig. 10b, $x/d_{\text{h}} = 4$ in Fig. 10c, $x/d_{\text{h}} = 6$ in Fig. 10d and $x/d_{\text{h}} = 8$ in Fig. 10e.

D. Turbulence intensity

The turbulence intensity is used as a method to evaluate the root-mean-square (RMS) value for the velocity fluctuations and is evaluated as

$$I = \frac{u_{\text{rms}}}{u_{\text{avg}}} = \sqrt{\frac{1}{3}\left(\langle u_x' \rangle^2 + \langle u_y' \rangle^2 + \langle u_z' \rangle^2\right)} \cdot \frac{1}{u_{\text{avg}}}\,. \tag{6}$$

Herein, the velocity fluctuations are the time-averaged velocity fluctuations defined by

$$\langle \boldsymbol{u}' \rangle^2 = \frac{1}{N}\sum_{i=0}^{N} \left(\boldsymbol{u} - \langle \boldsymbol{u} \rangle\right)^2\,. \tag{7}$$

The turbulence intensity is evaluated downstream of the pipe bend to analyse the turbulence induced and how it evolves as a function of the downstream length. Fig. 14 shows the turbulence intensity profiles at the outlet of the bend, $x = 0$, at a downstream distance of $x = 5d_{\text{h}}$ and close to the outlet of the computational domain, $x = 9d_{\text{h}}$. It is observed that the smallest bend radius induces the largest magnitude of turbu-

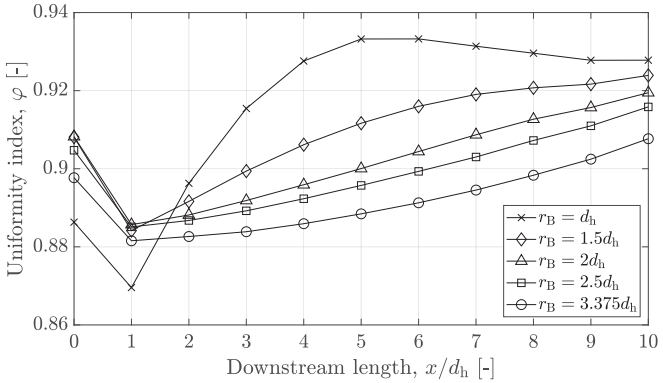

FIG. 11: Uniformity index, φ, for the velocity profile as a function of the pipe length.

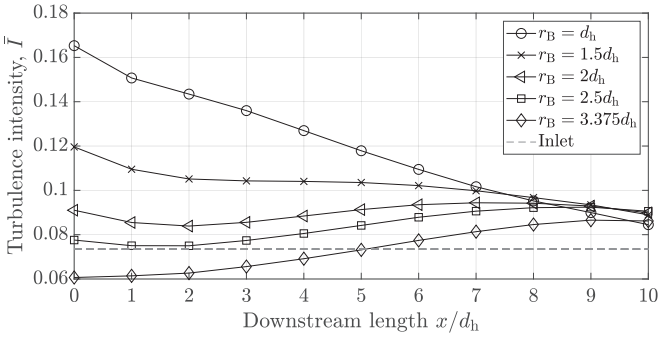

FIG. 12: Cross-sectional area-averaged turbulence intensity, $\bar{I}$, as a function of the length after the pipe bend for the different bend radii.

lence, shown in Fig. 14a. When the flow leaves the bend, a skewed turbulence intensity profile is observed for the two smallest bend radii. A larger turbulence intensity at the inner radius compared to the outer radius. Combining the turbulence intensity profile with the time-averaged velocity profile in Fig. 10 shows that the largest magnitude of turbulence intensity is induced at the location where the streamwise velocity is the lowest. As the bend radius increases, smaller magnitudes of turbulence intensity are observed at the outlet of the bend shown. Comparing the turbulence intensity profile at the outlet of the bend to the profile at the outlet of the domain shows that the turbulence decreases for the smallest bend radii and increases downstream of the bend for the largest bend radii. A decreasing magnitude of turbulence intensity is observed for the two smallest bend radii, $d_h \leq r_B \leq 1.5d_h$, in Fig. 14a and 14b. A relative small change is observed for the configuration with a bend radius of $r_B = 2d_h$ in Fig. 14c and an increasing trend is observed for the bend radii of $2d_h \leq r_B \leq 2.5d_h$ in Fig. 14d and 14e.

Averaging the turbulence intensity over the cross-sectional plane downstream of the bend shows how the evolution of the turbulence as a function of the downstream length. Fig. 12 shows the area-averaged turbulence intensity, $\bar{I}$, for the five different bend radii. As shown in the profile in Fig. 14, the simulation with the smallest bend radius induces significantly more turbulence at the outlet of the bend compared to the other configurations. The turbulence intensity for the smallest bend radius decreases with a larger gradient compared to the other bend radii, meaning that the turbulence dissipates faster at this configuration.

Another interesting observation, when analysing the area-averaged turbulence intensity is that the two simulations with the smallest bend radii, $r_B = d_h$ and $r_B = 1.5d_h$, both have a lower magnitude of turbulence intensity at the outlet of the pipe bend compared to the outlet of the domain. It is shown, in Fig. 10, how the velocity profile becomes skewed downstream of the bend as the bend radius increases. A higher velocity profile is observed at the outer radius of the pipe which serves to induce more turbulence which is shown in the turbulence intensity profile in Fig. 14. The configuration with a bend radius of $r_B = 2d_h$ remains almost constant downstream of the bend. This is also seen when analysing the turbulence intensity profile in Fig. 14c.

At the outlet of the computational domain, $x = 10d_h$, the area-averaged turbulence intensity for the configurations is between 8.4 % and 9 % . There is only a small difference between the different bend radii when observing the area-averaged turbulence intensity at the outlet of the domain. The smallest bend radii have the lowest value which is approaching the area-averaged turbulence intensity observed at the inlet. To achieve a turbulence intensity magnitude of the same order as is observed at the inlet, the downstream length would have to be extended to analyse at what position the impact of the upstream bend is negligible.

Combining the results from the area-averaged turbulence intensity in Fig. 12, the turbulence intensity profile in Fig. 14 and the uniformity index of the velocity profile in Fig. 11 provides information about the recovery length for the velocity profile. The turbulence intensity is largest at the outlet of the bend for the smallest bend radius and decays with the largest gradient. This configuration is also where the shortest recovery length is observed, which supports the indication of Hellström et al. (2013)[8] that the recovery of the velocity profile is driven by turbulent transport.

IV. CONCLUSION

In this study, large-eddy simulations have been carried out for a straight pipe with a length of $x = 10d_h$ followed by a 180° pipe bend which transitions to another straight pipe with a length of $x = 10d_h$ with the focus on studying the decay of secondary motion and turbulence intensity when having different bend radii. A total of 5 simulations are carried out with different bend radii, namely $r_B = d_h$, $r_B = 1.5d_h$, $r_B = 2d_h$, $r_B = 2.5d_h$ and $r_B = 3.375d_h$ at a Reynolds number of $Re_h = 10,000$. The numerical model is validated against experimental data presented by Toonder and Nieuwstadt (1997)[16] for the straight pipe section and against DNS data of Wang et al. (2018)[18] as well as experimental PIV-HS data of Sattarzadeh (2011)[19] and Kalpakli et al. (2016)[20] for 90° bend. Normalised velocity profiles and contours, secondary flow patterns, velocity profile uniformity index and

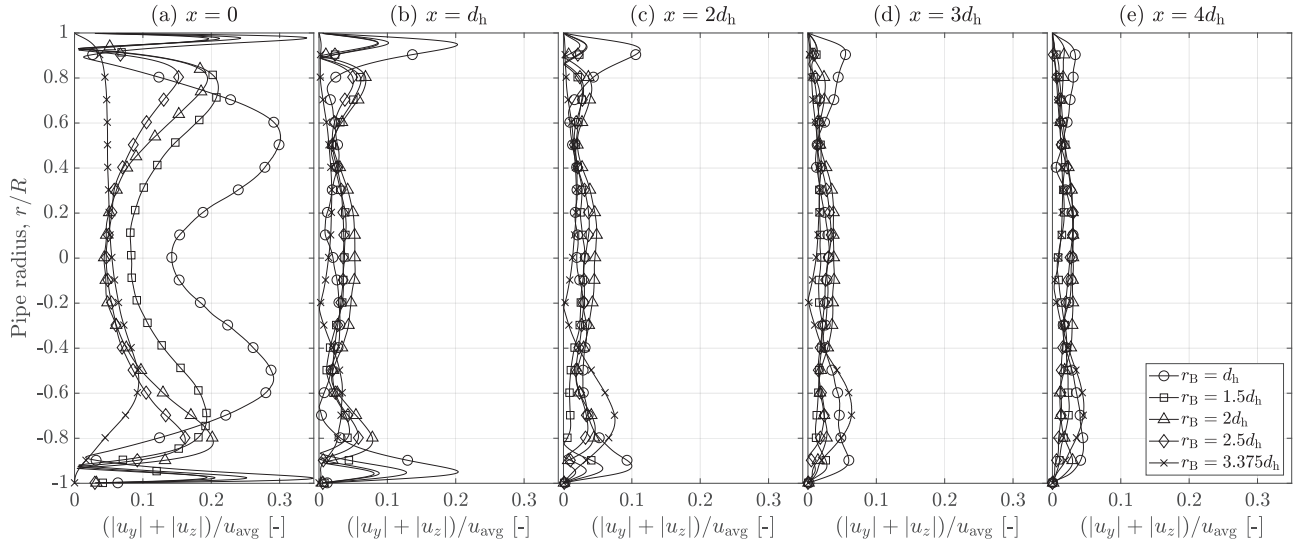

FIG. 13: Normalised secondary velocity, $\left(\left|u_y\right| + \left|u_z\right|\right)/u_{avg}$, at 13a: $x = 0$ after the pipe bend, 13b: $x = 1d_h$ after the pipe bend, 13c: $x = 2d_h$ after the pipe bend, 13d: $x = 3d_h$ after the pipe bend and 13e: $x = 4d_h$ after the pipe bend.

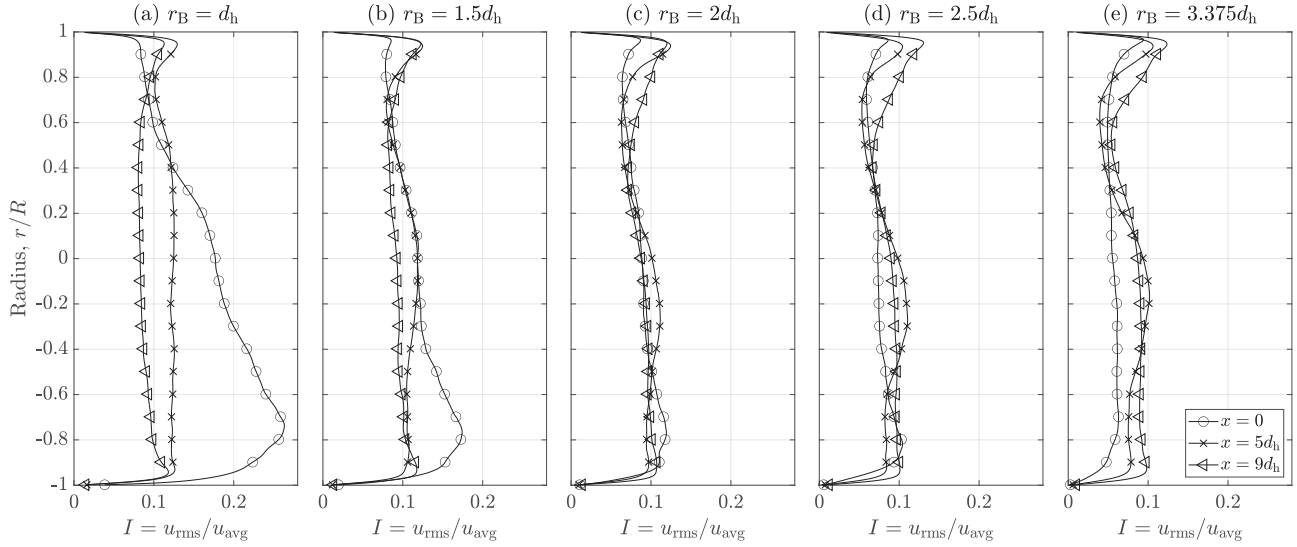

FIG. 14: Turbulence intensity profiles at the outlet of the bend, $x = 0$ and at downstream distances of $x = 5d_h$ and $x = 9d_h$ for a bend radius of $r_B = d_h$ in Fig. 14a, $r_B = 1.5d_h$ in Fig. 14b, $r_B = 2d_h$ in Fig. 14c, $r_B = 2.5d_h$ in Fig. 14d and $r_B = 3.375d_h$ in Fig. 14e. The inner pipe radius is defined by $r/R = -1$ and the outer is defined by $r/R = 1$.

turbulence intensity of the different bend radii are analysed downstream of the 180° bend.

The secondary flow vortices induced by the pipe bend increase in magnitude as the bend radius decreases. It shows how two peaks of secondary flow are dominating immediately after the bend and as the flow moves further downstream, the secondary flow is dominating closer to the walls. The normalised velocity profile becomes skewed with a higher normalised velocity at the outer radius of the bend as the flow is forced towards this outer radius. At the outlet of the bend, a small difference in the normalised velocity profiles is observed, meaning that the transition between the curvature of the bend and the straight pipe is an important factor in inducing downstream turbulence.

Like the increasing magnitude of secondary flow, the turbulence intensity increases as the bend radius decreases. For the two simulations with the smallest bend radii, $r_B = d_h$ and $r_B = 1.5d_h$, a decreasing gradient of turbulence intensity is observed downstream of the bend and an increasing gradient for the turbulence intensity is observed for the two simulations with the largest bend radii, $r_B \geq 2.5d_h$. It is shown that the large magnitude of induced turbulence at the outlet of the bend, causes the velocity profile to recover faster, as the uniformity index of the velocity profile increases faster for the smallest bend radius. As the turbulence dissipates with a larger gradient, the velocity profile recovers over a shorter dis-

tance. This observation supports the statement of Hellström et al. (2013)[8], who state that the recovery of the velocity profile is driven by turbulence transport.

ACKNOWLEDGEMENTS

The authors would like to express their acknowledgement to Anders Schou Simonsen who contributed to this work with great input and comments.

Funding

This work is financially supported by the Danish Innovation Foundation under grant no. 9065-00188B.

Declaration of interest

The authors declare that they have no conflict of interest.

[1] J. Kim, M. Yadav, and S. Kim, "Characteristics of Secondary Flow Induced by 90-Degree Elbow in Turbulent Pipe Flow," Engineering Applications of Computational Fluid Mechanics **8**, 229–239 (2014).

[2] A. L. S. Salustiano Martim, J. G. Dalfré Filho, Y. d. F. L. De Lucca, and A. I. Borri Genovez, "Electromagnetic flowmeter evaluation in real facilities: Velocity profiles and error analysis," Flow Measurement and Instrumentation **66**, 44–49 (2019).

[3] M. Rowe, "Measurements and computations of flow in pipe bends," Journal of Fluid Mechanics **43**, 771–783 (1970).

[4] J. Azzola, J. A. Humphrey, H. lacovides, and B. E. Launder, "Developing turbulent flow in a u-bend of circular cross-section: Measurement and computation," Journal of Fluids Engineering, Transactions of the ASME **108**, 214–221 (1986).

[5] B. E. Launder and D. B. Spalding, "The numerical computation of turbulent flows," Computer Methods in Applied Mechanics and Engineering **3**, 269–289 (1974).

[6] K. Sudo, M. Sumida, and H. Hibara, "Experimental investigation on turbulent flow through a circular-sectioned 180° bend," Experiments in Fluids **28**, 51–57 (2001).

[7] K. Sudo, M. Sumida, and H. Hibara, "Experimental investigation on turbulent flow in a circular-sectioned 90-degree bend," Experiments in Fluids **25**, 42–49 (1998).

[8] L. H. Hellström, M. B. Zlatinov, G. Cao, and A. J. Smits, "Turbulent pipe flow downstream of a 90° bend," Journal of Fluid Mechanics **735**, R7 (2013).

[9] M. Di Liberto, I. Di Piazza, and M. Ciofalo, "Turbulence structure and budgets in curved pipes," Computers and Fluids **88**, 452–472 (2013).

[10] R. Röhrig, S. Jakirlić, and C. Tropea, "Comparative computational study of turbulent flow in a 90° pipe elbow," International Journal of Heat and Fluid Flow **55**, 120–131 (2015).

[11] E. Gotfredsen, J. D. Kunoy, S. Mayer, and K. E. Meyer, "Experimental validation of RANS and DES modelling of pipe flow mixing," Heat and Mass Transfer/Waerme- und Stoffuebertragung , 2211–2224 (2020).

[12] R. I. Issa, "Solution of the implicitly discretised fluid flow equations by operator-splitting," Journal of Computational Physics **62**, 40–65 (1986).

[13] F. Nicoud and F. Ducros, "Subgrid-Scale Stress Modelling Based on the Square of the Velocity Gradient Tensor," Flow, Turbulence and Combustion **62**, 183–200 (1999).

[14] S. K. Robinson, "Coherent motions in the turbulent boundary layer," Annual Review of Fluid Mechanics **23**, 601–639 (1991).

[15] J. Hærvig, K. Sørensen, and T. J. Condra, "Early stages of agglomeration of adhesive particles in fully-developed turbulent pipe flows," International Journal of Multiphase Flow **106**, 254–267 (2018).

[16] D. Toonder and J. M. J. Nieuwstadt, "Reynolds number effects in a turbulent pipe flow for low to moderate Re," Physics of Fluids **9**, 3398–3409 (1997).

[17] T. Von Kármán, "Mechanische Ähnlichkeit und Turbulenz," Göttinger Nachr , 58–76 (1930).

[18] Z. Wang, R. Örlü, P. Schlatter, and Y. M. Chung, "Direct numerical simulation of a turbulent 90° bend pipe flow," International Journal of Heat and Fluid Flow **73**, 199–208 (2018).

[19] S. S. Sattarzadeh, *Experimental study of complex pipe flows*, Ph.D. thesis, KTH Mechanics (2011).

[20] A. Kalpakli Vester, S. S. Sattarzadeh, and R. Örlü, "Combined hot-wire and PIV measurements of a swirling turbulent flow at the exit of a 90° pipe bend," Journal of Visualization **19**, 261–273 (2016).

[21] W. Dean, "The stream-line motion of fluid in a curved pipe," The London, Edinburgh, and Dublin Philosophical Magazine and Journal of Science **5**, 673–695 (1928).

[22] M. Anwer, R. M. So, and Y. G. Lai, "Perturbation by and recovery from bend curvature of a fully developed turbulent pipe flow," Physics of Fluids A **1**, 1387–1397 (1989).

[23] A. Kalpakli and R. Örlü, "Turbulent pipe flow downstream a 90° pipe bend with and without superimposed swirl," International Journal of Heat and Fluid Flow **41**, 103–111 (2013).